Advanced Powder Technology 33 (2022) 103793

Contents lists available at ScienceDirect

Advanced Powder Technology

journal homepage: www.elsevier.com/locate/apt

Original Research Paper

Detailed analysis of particle–substrate interaction based on a centrifugal method

Shunto Kinugasa, Shuya Tanoue, Yasuhiro Shimada, Shuji Matsusaka *

Department of Chemical Engineering, Kyoto University, Kyoto 615-8510, Japan

ARTICLE INFO

Article history:
Received 6 June 2022
Received in revised form 31 August 2022
Accepted 8 September 2022
Available online 18 October 2022

Keywords:
Centrifugal method
Point-mass model
Rigid-body model
Particle adhesion force
Effective contact radius

ABSTRACT

The interaction between particles and inclined substrates in a centrifuge was investigated theoretically and experimentally. First, the balance of the force acting on a particle adhering to the substrate, with an inclination angle from 0 to 90° to the horizontal, was formulated separately in the normal and tangential directions. The adhesion force was then derived based on the point-mass model as a function of the angular velocity. Next, the balance of the moments of the forces acting on a particle adhering to the substrate was formulated; theoretical equations for the adhesion force and the effective contact radius were then derived from the angular velocities, obtained at any two inclination angles, based on the rigid-body model. Finally, the removal fraction curves of spherical/nonspherical particles with median diameters of less than 10 μm were experimentally obtained by increasing the angular velocity at each inclination angle. The experimentally obtained angular velocities were substituted into the theoretical equations to compare the point-mass and rigid-body models. The effects of the particle shape on the adhesion force and effective contact radius and that of the inclination angle on the removal fraction curves based on the theoretical equation were also investigated.

1. Introduction

Particle adhesion occurs as a result of particle–particle and particle–wall interactions [1] and causes blockages, flow fluctuations, and other issues during powder storage, feeding, and conveying [2]. To solve these problems, it is necessary to determine and evaluate the adhesion force of the particles.

The adhesion force can be measured using several methods, such as the spring balance, centrifugation, vibration, and airflow methods [3]. The colloidal probe method that uses an atomic force microscope (AFM) [4] and the spring balance method that uses a contact needle [5] have the advantage of directly measuring the adhesion force. However, these methods are not suitable for the statistical analysis of the adhesion forces of many particles because only a single particle can be measured in one operation. In contrast, the centrifugation, vibration, and airflow methods can measure numerous particles simultaneously and can be applied to particles with a wide distribution of adhesion forces. In particular, the centrifugal method uses an external force that does not vary with time, which allows for a proper analysis of the limit of particle separation.

Studies on the centrifugal method have been conducted since the 1960s [6,7]. The effects of the particle conditions, such as material, size, shape, and surface roughness; substrate conditions, such as the material and surface roughness; and operating conditions, such as the contact time and initial load on the adhesion force, have been reported quantitatively [8–14]. In addition, the adhesion forces measured by the centrifugal method have been compared with their theoretical values [9,11]. Recently, some studies have also analyzed the various factors affecting adhesion by introducing an 'effective Hamaker constant' into the van der Waals force [12–14].

In general, the substrates to which the particles are attached are arranged such that the centrifugal forces pull the particles apart. This arrangement is considered the standard method for measuring particle adhesion forces [15]. Moreover, in the study by Podczeck et al., the substrates were inclined from the direction of rotation to evaluate the adhesion and friction forces [16].

Conventionally, adhesion and friction forces have been analyzed by assuming that particles are point masses; thus, the effects of the particle and contact area sizes are not reflected in the measurement results. For an advanced analysis, the particles should be ana-

* Corresponding author.
E-mail address: matsu@cheme.kyoto-u.ac.jp (S. Matsusaka).

https://doi.org/10.1016/j.apt.2022.103793

Nomenclature

a	effective contact radius between particle and substrate, m	R_a	arithmetic mean height, m
C_{50}	count median circularity of particles	R_{Sm}	mean width of profile elements, m
D_p	particle diameter, m	r	centrifugal radius, m
D_{p50}	count median diameter of particles, m	β	inclination angle from horizontal, rad
E	Young's modulus, Pa	η	Number-based removal fraction
F	cumulative distribution function	θ	half-apex angle, rad
F_a	adhesion force, N	μ	static friction coefficient
F_f	friction force, N	ν	Poisson's ratio
g	gravitational acceleration, m/s^2	ρ_p	particle density, kg/m^3
M_c	moment of force, N·m	σ_g	geometric standard deviation of particle size distribution
m_p	particle mass, kg		
N	normal force, N	ω	angular velocity, rad/s

lyzed as rigid bodies [17], which allows for the analysis of the rotational motion of the particles, in addition to their translational motion, by using the moment of force.

The superiority of the rigid-body model was demonstrated in experiments in which the substrates were placed both horizontally and vertically in a centrifuge [18]. The rigid-body model was subsequently applied to evaluate the adhesion forces under conditions that included the effects of the nonspherical particles and surface roughness [19,20]. Focusing on the difference in the angular velocity for particle removal between the horizontal and vertical substrates, theoretical equations for analyzing the adhesion force and effective contact radius have also been presented, based on the balance of the moments of forces acting on the particles [3].

After experimentally validating the rigid-body model, Shimada et al. [21] substituted the two centrifugation angular velocities obtained with horizontal and vertical substrates into the theoretical equation. The researchers reported the dependence of the particle size, substrate surface roughness, relative humidity, and initial load on both the adhesion force and effective contact radius. However, to the best of our knowledge, to date, no extension to substrates, inclined at angles other than the horizontal and vertical has been made, nor have detailed theoretical investigations of point-mass and rigid-body models been conducted.

In this study, the balance of the force acting on a particle adhering to a substrate with an inclination angle ranging from 0 to 90° to the horizontal was formulated, based on the centrifugal method. Subsequently, a theoretical equation for the adhesion force from the angular velocity was derived based on the point-mass model. Theoretical equations for the adhesion force and the effective contact radius from the angular velocities, obtained at any two inclination angles were also derived based on the rigid-body model. The removal fraction curves of the spherical and nonspherical particles were obtained by increasing the angular velocity at different inclination angles. Subsequently, the angular velocities were substituted into the theoretical equations to compare the point-mass and rigid-body models. In addition, the effects of particle shape on the adhesion force and effective contact radius and that of the inclination angle on the removal fraction curves are also discussed herein.

2. Mechanism of particle removal from substrates

Fig. 1 shows the forces acting on the particles (with diameter D_p and mass m_p) adhering to an inclined substrate rotating at an angular velocity ω. It is assumed that the surface of the inclined substrate is slightly rough, and that the particles are in contact at multiple points with the substrate at an inclination angle β. The spherical particles are depicted in Fig. 1 (a) and (b), while the irregularly shaped particles are shown in Fig. 1 (c) and (d).

Fig. 1(a) and (c) show the point-mass models considering friction with gravity $m_p g$ in the vertical direction and centrifugal force $m_p r\omega^2$ in the horizontal direction, where r is the centrifugal radius. The adhesion force F_a and normal force N act in the direction normal to the substrate, while the friction force F_f acts in the tangential direction. Here, it is assumed that the particles slide on an inclined substrate without rolling. In contrast, Fig. 1(b) and (d) show rigid-body models in which the particle is assumed to roll on the substrate. Although the actual contact state is complex, considering a half-apex angle θ, the effective contact radius a can be expressed as:

$$a = \frac{D_p}{2}\sin\theta \tag{1}$$

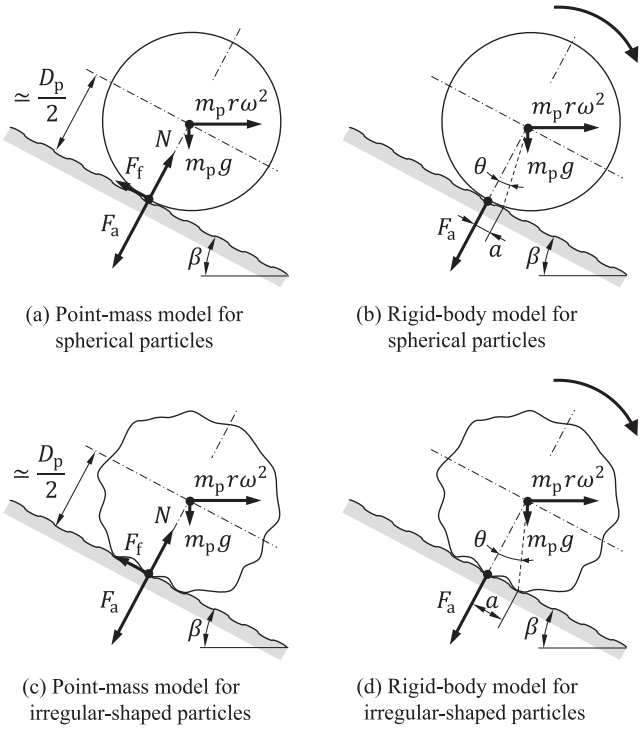

(a) Point-mass model for spherical particles

(b) Rigid-body model for spherical particles

(c) Point-mass model for irregular-shaped particles

(d) Rigid-body model for irregular-shaped particles

Fig. 1. Forces acting on particles adhering to slightly rough substrate surfaces placed at an angle in the centrifuge.

2.1. Point-mass model

The combined forces in the normal direction of the particles adhering to the substrate are expressed as:

$$F_a - N = m_p(r\omega^2 \sin\beta - g\cos\beta) \tag{2}$$

Assuming that the forces acting in the normal direction dominate particle removal, the condition $N = 0$ is added. Thus, Eq. (2) may be transformed into:

$$F_a = m_p(r\omega^2 \sin\beta - g\cos\beta) \tag{3}$$

When $\beta = 90°$, Eq. (3) becomes:

$$F_a = m_p r\omega^2 \tag{4}$$

Next, assuming that the tangential forces remove the particles, the critical state can be expressed as:

$$F_f = \mu N = m_p(r\omega^2 \cos\beta + g\sin\beta) \tag{5}$$

Where μ is the static friction coefficient. Combining Eqs. (2) and (5) yields:

$$F_a = m_p\left\{r\omega^2 \sin\beta - g\cos\beta + \frac{r\omega^2\cos\beta + g\sin\beta}{\mu}\right\}$$

$$= m_p\left\{r\omega^2\left(\frac{\cos\beta}{\mu} + \sin\beta\right) + g\left(\frac{\sin\beta}{\mu} - \cos\beta\right)\right\} \tag{6}$$

The comparison of Eqs. (3) and (6) under the condition $0 \le \beta \le 90°$ shows that Eq. (6) can be used to remove particles comprising greater adhesion forces at the same angular velocity. The equation can also be used to remove particles with the same adhesion force at lower angular velocities. Therefore, the tangential forces dominate particle removal. Furthermore, substituting $\beta = 90°$ into Eq. (6) yields:

$$F_a = m_p\left(r\omega^2 + \frac{g}{\mu}\right) \tag{7}$$

A comparison of Eqs. (4) and (7) indicates that the latter can be used for the particle removal mechanism, meaning that the tangential forces dominate particle removal even at $\beta = 90°$. However, by adding the condition $r\omega^2 \gg g$, Eq. (7) becomes:

$$F_a = m_p r\omega^2 \tag{8}$$

Notably, Eq. (8) is the same as Eq. (4).

When $\beta = 0$, Eq. (6) becomes:

$$F_a = m_p\left(\frac{r\omega^2}{\mu} - g\right) \tag{9}$$

By adding the condition $r\omega^2 \gg g$, Eq. (9) becomes:

$$F_a = \frac{m_p r\omega^2}{\mu} \tag{10}$$

2.2. Rigid-body model

The moments of the forces acting on the particles shown in Fig. 1 are expressed as:

$$\{F_a - m_p(r\omega^2 \sin\beta - g\cos\beta)\}a \approx m_p(r\omega^2\cos\beta + g\sin\beta)\frac{D_p}{2} \tag{11}$$

Here, the perpendicular distance for the clockwise moments of the forces is approximated by $D_p/2$. Solving Eq. (11), F_a can be expressed as:

$$F_a \approx m_p\left\{r\omega^2 \sin\beta - g\cos\beta + (r\omega^2\cos\beta + g\sin\beta)\frac{D_p}{2a}\right\}$$

$$\approx m_p\left\{r\omega^2\left(\frac{D_p}{2a}\cos\beta + \sin\beta\right) + g\left(\frac{D_p}{2a}\sin\beta - \cos\beta\right)\right\} \tag{12}$$

In the rigid-body model, there are two unknowns, namely F_a and a. Assuming that these are independent of the inclination angle, the equations for these unknowns can be derived by using two inclination angles, β_1 and β_2, and their corresponding particle removal angular velocities, ω_1 and ω_2, as follows (see Appendix):

$$F_a \approx m_p \times \frac{\left\{(r\omega_1\omega_2)^2 + g^2\right\}\sin(\beta_2 - \beta_1) + gr(\omega_2^2 - \omega_1^2)\cos(\beta_2 - \beta_1)}{r(\omega_1^2\cos\beta_1 - \omega_2^2\cos\beta_2) + g(\sin\beta_1 - \sin\beta_2)} \tag{13}$$

$$a \approx \frac{D_p}{2}\frac{r(\omega_1^2\cos\beta_1 - \omega_2^2\cos\beta_2) + g(\sin\beta_1 - \sin\beta_2)}{r(-\omega_1^2\sin\beta_1 + \omega_2^2\sin\beta_2) + g(\cos\beta_1 - \cos\beta_2)} \tag{14}$$

When $\beta_1 = 0$ and $\beta_2 = 90°$, Eqs. (13) and (14), respectively, become:

$$F_a \approx m_p\frac{(r\omega_1\omega_2)^2 + g^2}{r\omega_1^2 - g} \tag{15}$$

$$a \approx \frac{D_p}{2}\cdot\frac{r\omega_1^2 - g}{r\omega_2^2 + g} \tag{16}$$

By adding the condition $r\omega^2 \gg g$, Eqs. (15) and (16), respectively, become:

$$F_a \approx m_p r\omega_2^2 \tag{17}$$

$$a \approx \frac{D_p}{2}\left(\frac{\omega_1}{\omega_2}\right)^2 \tag{18}$$

2.3. Comparison of point-mass and rigid-body models

Eqs. (6) and (12), which are used to determine the adhesion force, show that the difference between the point-mass and rigid-body models lies in the static friction coefficient μ and the ratio of the effective contact radius to the particle radius $2a/D_p$. For $\mu < 2a/D_p$, it is appropriate to apply the point-mass model, while the rigid-body model is more suitable for $\mu > 2a/D_p$. Furthermore, since Eq. (17) is equivalent to Eq. (8), the point-mass model can be substituted for the rigid-body model when the conditions $\beta = 90°$ and $r\omega^2 \gg g$ are satisfied. Notably, here the rigid-body model is essential for analyzing the effective contact radius a.

3. Experimental setup and methods

A centrifuge (CT15E; Eppendorf Himac Technologies Co., Ltd.) has a vertical axis of rotation, wherein the sample rotates in the horizontal plane. In the experiment, the rotor was covered with a tight lid so that no airflow was generated inside the rotor, thus implying that no aerodynamic effects occurred. The centrifugal radius of the small area used for measuring the removal fraction of the particles adhering to the substrate was 66 mm. The centrifuge speed was increased from 300 to 15,000 rpm (i.e., from 10 π to 500 π rad/s) in 100 rpm increments under atmospheric pressure. The inclination angles of the substrate to which the particles were attached were set at $\beta = 10$, 40, 60, 80, and 90° from the horizontal. Horizontal substrates with $\beta = 0$ were excluded from the experimental conditions to avoid the possibility that any particles removed by centrifugal force could cause excessive particle removal due to collision with other particles.

Two types of sample particles were employed, namely glass beads (9000 series; Thermo Fisher Scientific, Inc.) and copper

particles (Fukuda Metal Foil and Powder Co., Ltd.). Mirror-finished SUS304 stainless steel plates were used as the substrates to which the particles were attached. The substrates were washed with ethanol and allowed to dry naturally prior to use. The particle dispersion system of a particle image analyzer (Morphologi G3; Malvern Instruments Ltd.) was used to disperse and adhere the particles to the substrate surface. The pressure of the air used for particle dispersion was 100 kPa. The area occupancy of the particles—the ratio of the projected area of all the particles to the substrate surface in an area of 0.25 mm^2— was less than 4%.

After photographing the particles adhering to the substrate, the substrate was fixed in the centrifuge at a given inclination angle. The centrifugation and photography were repeated while increasing the angular velocity stepwise, with each centrifugation lasting 1 min. The captured images were binarized using particle count analysis software (VT-A100S; Nano Seeds Corp.) to measure the number of particles, and number-based removal fraction curves were subsequently obtained. The experiments were conducted at a temperature of 23 ± 5 °C and relative humidity of 35 ± 13%.

4. Results and discussion

4.1. Shape and size distributions of sample particles

Fig. 2 shows the typical scanning electron microscopy (SEM) images of the two types of sample particles used. The glass beads were spherical with relatively smooth surfaces, while the copper particles were irregularly shaped with rough surfaces.

Fig. 3 shows the number-based cumulative particle size distributions of the glass beads and copper particles measured using the particle image analyzer. The particle size distributions of the two samples were both relatively narrow, with the copper particles displaying a slightly wider distribution than that of the glass beads. Median diameters of less than 10 μm were observed for both the glass beads and copper particles. The median diameter of each sample was used as the representative particle diameter in the analysis [15,21]. Table 1 summarizes the values of the count median diameter D_{p50}, geometric standard deviation σ_g, count median circularity C_{50}, particle density ρ_p, Young's modulus E, and Poisson's ratio ν.

4.2. Surface condition of sample substrate

Fig. 4 shows an image of the substrate captured using a laser microscope (LEXT-OLS4100; Olympus). The image reveals a slightly rough surface; however, no specific directionality in the shape and arrangement of the roughness were observed. Table 2 summarizes the arithmetic mean height R_a, mean width of the profile elements R_{Sm}, Young's modulus E, and Poisson's ratio ν of the substrate.

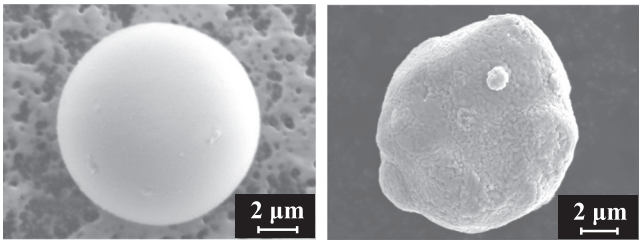

(a) Glass (b) Copper

Fig. 2. SEM images of the sample particles.

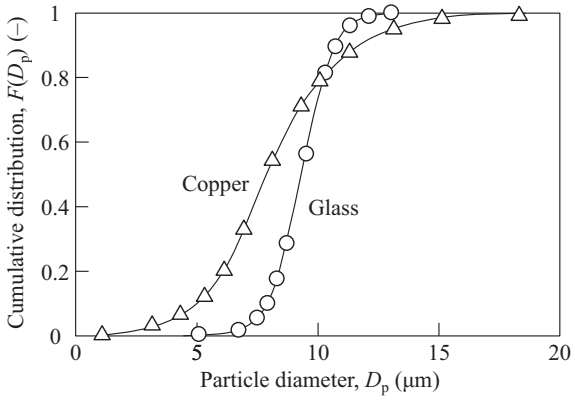

Fig. 3. Number-based particle size distribution.

Table 1
Properties of the particles.

Sample	Glass beads	Copper particles
D_{p50} (μm)	9.4	8.0
σ_g (–)	1.12	1.36
C_{50} (–)	0.993	0.987
ρ_p (kg/m^3)	2530	4750
E (Pa)	7.24×10^{10}	1.30×10^{11}
ν (–)	0.22	0.34

Fig. 4. Enlarged image of the substrate surface.

Table 2
Properties of the stainless steel plate substrate.

R_a (μm)	R_{Sm} (μm)	E (Pa)	ν (–)
0.01	11.2	2.2×10^{11}	0.29

4.3. Experimental removal fraction

Fig. 5(a) shows the experimental removal fraction of the glass beads on the substrates with different inclination angles as a function of the angular velocity. Each removal fraction curve was obtained by counting more than 400 particles. The results reveal that the removal fraction increases with an increase in the angular velocity but decreases with an increase in the inclination angle. This trend is also observed for the copper particles, as shown in Fig. 5(b). However, the copper particles display lower angular velocities than the glass beads, revealing differences in the removal

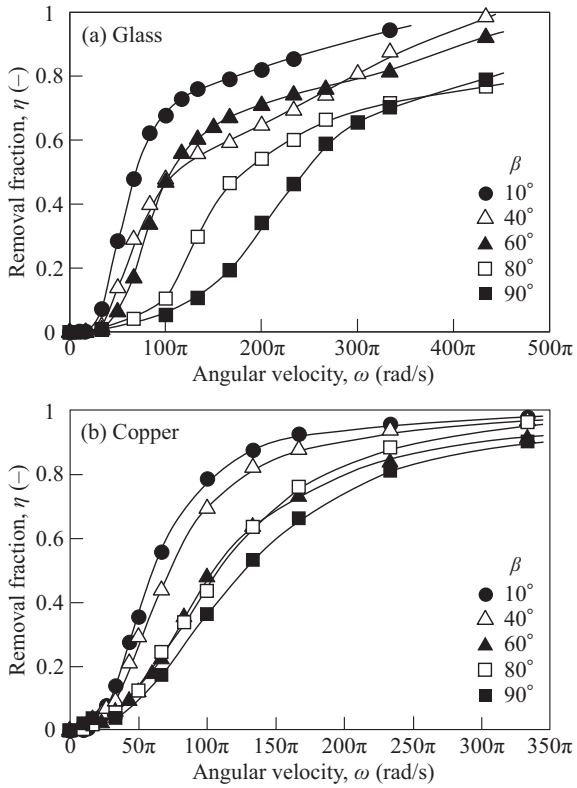

Fig. 5. Experimental removal fraction as a parameter of the inclination angle.

fraction depending on the sample type. This phenomenon is discussed in greater detail in Section 4.4 below.

4.4. Analysis using point-mass model

Fig. 6 shows the adhesion forces based on the point-mass model, obtained by substituting the angular velocities at β = 10 and 90° into Eq. (6). Fig. 6(a) and (b) respectively show the results obtained for the glass beads and copper particles. The ω values used in the calculations were obtained at 10% intervals at a removal fraction of 10% or greater, using the experimental lines in Fig. 5(a) and (b), because the removal fractions for β = 10 and 90° had to be the same. The particle mass was obtained from the count median diameter and particle density. Static friction coefficients μ of 0.26 [18] and 0.55 [22] were used for the glass beads and copper particles, respectively. The results reveal that the adhesion force increases at a higher removal fraction for both sample types, indicating that the particles with smaller adhesion forces are removed earlier. Moreover, the adhesion force increases significantly as the removal fraction increases, indicating that a certain number of particles displays very high adhesion forces.

The adhesion force at β = 10° was predicted to be smaller than that at β = 90°; however, these two values should be the same. Therefore, we concluded that the adhesion force at β = 10° was underestimated, and the point-mass model did not properly predict the values. This result suggests that the particles did not slide with friction, but rather rolled on the inclined substrate, as discussed in more detail in Section 4.5 below.

Finally, a comparison of the glass beads and copper particles shows that the latter presents smaller adhesion forces. This may be due to the rough surface of the copper particles, which results in a larger gap between the contact surfaces [23,24].

4.5. Analysis using rigid-body model

Fig. 7 shows the adhesion forces based on the rigid-body model obtained by substituting two different ω values into Eq. (13). It is desirable to use ω values for two significantly different inclination angles to improve the estimation accuracy of the adhesion force. Therefore, in the experiment, we used ω values with β = 10 and 90°, as illustrated in Fig. 5(a) and (b), respectively. The results reveal that the adhesion force distributions obtained with the rigid-body model are similar to those obtained with the point-mass model at β = 90° (Fig. 6). Thus, although the rigid-body model is essential for analyzing the effective contact radius, it is confirmed that at β = 90° and $r\omega^2 \gg g$, the point-mass model can be employed to estimate the adhesion force instead of the rigid-body model.

4.6. Effective contact radius

Fig. 8 shows the effective contact radii obtained by substituting two ω values into Eq. (14). The effective contact radius between the glass beads and substrate is distributed in the range of 0.3–0.7 μm. This corresponds to 6–15% of the particle radius, that is, $2a/D_p$ = 0.06–0.15. However, the effective contact radius between the copper particles and substrate is distributed in the range of 0.7–1.4 μm. This corresponds to 18–35% of the particle radius, that is, $2a/D_p$ = 0.18–0.35. Conversion to the half-apex angles, which are an indicator of the contact states, affords values of 4–9° for the glass beads and 10–20° for the copper particles. These results indicate that the effective contact radii of the copper particles are larger than those of the glass beads, even though the median diameter of the glass beads is relatively larger. This may be due to the irregular shape of the copper particles, whereas the glass beads are near-spherical. Both sample particles exhibit $\mu > 2a/D_p$, which verifies that the point-mass model is inappropriate for small inclination angles, and thus, the rigid-body model must be used under such conditions.

The effective contact radius increases with increasing removal fraction for the glass beads and decreases for the copper particles. Unfortunately, because the effective contact radius could be complexly affected by the particle size, particle shape, surface roughness, and their respective distributions, the trends in the removal fraction were not able to be uniquely determined.

4.7. Simulated removal fraction

The effect of the inclination angle on the removal fraction can also be studied theoretically. From Eq. (12), the angular velocity ω required to remove particles can be derived as a function of the inclination angle as follows:

$$\omega \approx \sqrt{\frac{\frac{F_a}{m_p} - g\left(\frac{D_p}{2a}\sin\beta - \cos\beta\right)}{r\left(\frac{D_p}{2a}\cos\beta + \sin\beta\right)}} \tag{19}$$

The F_a values at each removal fraction for the glass beads and copper particles were determined from Fig. 7. For simplicity, the a values were maintained at 0.35 μm for the glass beads and 0.95 μm for the copper particles, referring to Fig. 8.

Fig. 9 shows the results calculated using Eq. (19). Similar to the experimental results in Fig. 5, the removal fraction increases with an increase in the angular velocity but decreases with an increase in the inclination angle. Notably, as β increases, the effect of β on the removal fraction becomes more prominent. This is because β affects the moment of the centrifugal force M_c. Based on the rigid-body model shown in Eq. (11), M_c can be expressed as:

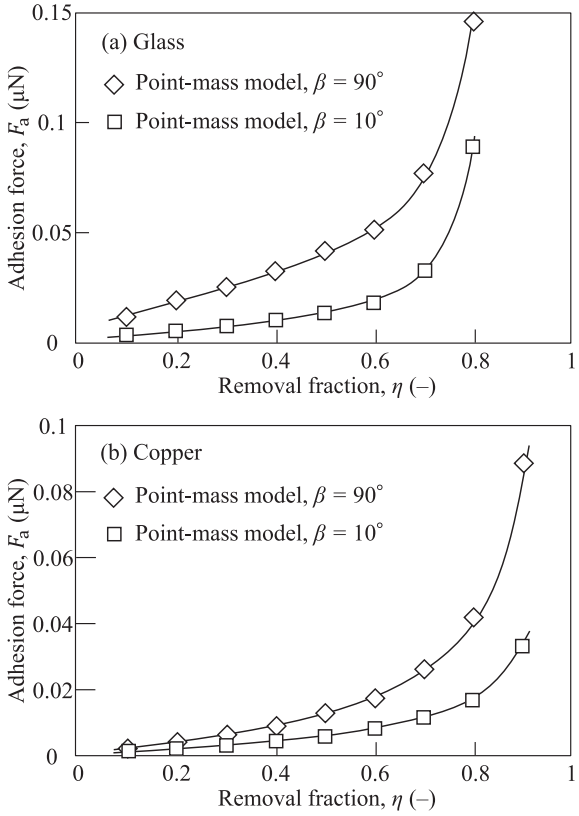

Fig. 6. Adhesion force obtained by the point-mass model.

$$M_c \approx m_p r\omega^2 \left(\frac{D_p}{2}\cos\beta + a\sin\beta\right) \tag{20}$$

When β approaches 90° under the condition $D_p > a$, the effect of the decrease in $(D_p/2)\cos\beta$ is greater than that of the increase in $a\sin\beta$. Thus, we conclude that ω must be increased to ensure that the M_c value required to remove particles is attained.

A comparison of the glass beads and copper particles shows that the latter display a lower rate of change in ω with a change in β. This is because the copper particles have larger a values, and thus, ω no longer needs to be increased significantly. Fig. 9 also shows that the effect of β on ω is very small when β is less than 30°, indicating that it is not necessary to limit the minimum β value to 0 as a condition for the analysis with two β values.

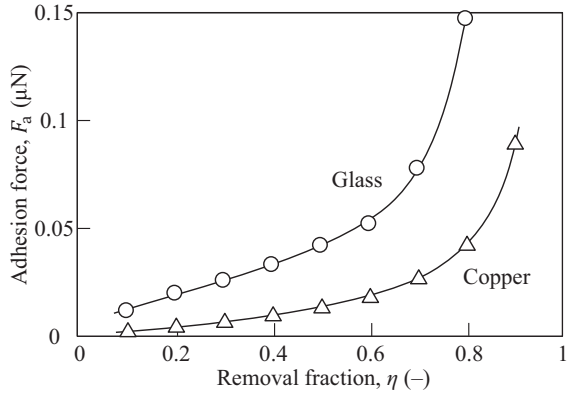

Fig. 7. Adhesion force obtained by the rigid-body model.

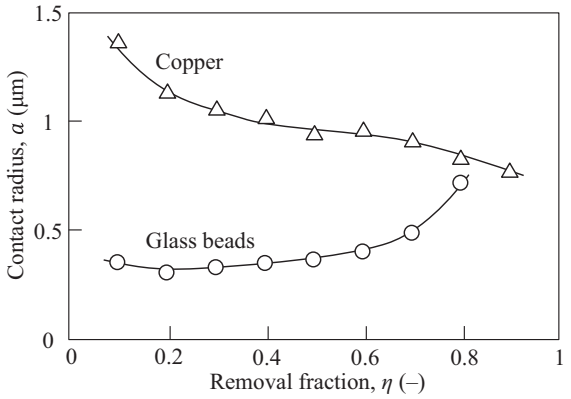

Fig. 8. Contact radius obtained by the rigid-body model.

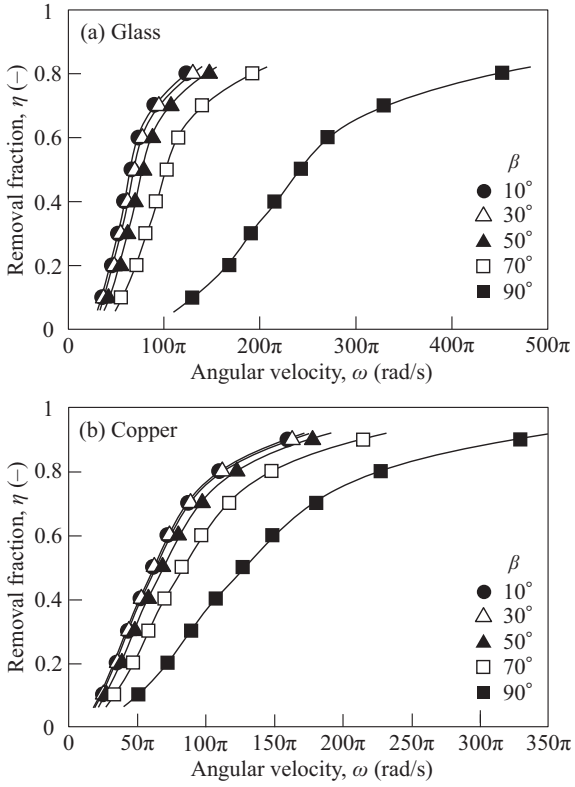

Fig. 9. Simulated removal fraction as a parameter of the inclination angle.

5. Conclusions

In this study, two models, the point-mass and rigid-body models, were used to theoretically investigate the removal mechanism of particles adhering to a substrate with an inclination angle (β = 0–90°) to the horizontal in a centrifuge, which had a vertical axis of rotation and rotated in the horizontal plane. Furthermore, experiments were conducted to centrifuge two types of particles—spherical glass beads with smooth surfaces and a median diameter of 9.4 μm and irregularly shaped copper particles with rough surfaces and a median diameter of 8.0 μm—from a substrate with a slightly rough surface. The conclusions made from this study are as follows:

1) Formulation of the respective combined forces, normal and tangential to the substrate, using the point-mass model reveals that the particle removal is dominated by tangential forces under the condition $0 \leq \beta \leq 90°$. However, by adding the conditions $\beta = 90°$ and $r\omega^2 \gg g$, the equation for the balance of forces in the tangential direction becomes the same as the normal.
2) In the rigid-body model, the balance of the moments of forces can be formulated by introducing the effective contact radius as the spread of the contact area between the particle and substrate. In this formulation, the unknowns are the adhesion force and effective contact radius, both of which can be solved using the centrifugal acceleration values at two different inclination angles.
3) The static friction coefficient μ is the essential factor in the point-mass model for removing particles from the inclined substrates. In contrast, for the rigid-body model, the ratio of the effective contact radius to the particle radius, $2a/D_p$, is the essential factor. Under the condition $\mu < 2a/D_p$, it is appropriate to apply the point-mass model, while for $\mu > 2a/D_p$, the rigid-body model is more appropriate. By adding the conditions $\beta = 90°$ and $r\omega^2 \gg g$, the rigid-body model for adhesion force estimation can be substituted with the point-mass model. Hence, the rigid-body model is essential for analyzing the effective contact radius.
4) The experimental results show that the particle removal fraction increases with an increase in the angular velocity but decreases with an increase in the inclination angle.
5) When the experimental results at $\beta = 10°$ are analyzed using the point-mass model, the adhesion force is underestimated. This suggests that the particles do not slide against friction but rather roll on the inclined substrate.
6) The adhesion force of the copper particles is smaller than that of the glass beads. This may be due to the rough surface of the copper particles, which results in a larger gap between the contact surfaces.
7) The adhesion force distributions obtained from the rigid-body model analysis of the experiments conducted at β = 10 and 90° are similar to those obtained using the point-mass model at $\beta = 90°$. This supports the theory that the point-mass model at $\beta = 90°$ and $r\omega^2 \gg g$ can be substituted for the rigid-body model.
8) According to the rigid-body model analysis, the effective contact radius between the glass beads and substrate is in the range of 0.3–0.7 μm (i.e., $2a/D_p$ = 0.06–0.15), while that between the copper particles and substrate is in the range of 0.7–1.4 μm (i.e., $2a/D_p$ = 0.18–0.35). Therefore, the effective contact radii of the copper particles are larger than those of the glass beads, even though the median diameter of the glass beads is relatively larger. This may be due to the irregular shape of the copper particles. Both sample particles exhibit $\mu > 2a/D_p$, which confirms that the rigid-body model must be used for small inclination angles.
9) The angular velocity required to remove particles can be derived from the rigid-body model as a function of the inclination angle β. This theoretical analysis explains the experimental results that the effect of β on the removal fraction becomes more prominent as β increases. Furthermore, because the effect of β on the angular velocity is very small at $\beta \leq 30°$, it is not necessary to limit the minimum β value to 0 as a condition for the analysis with two β values.

Declaration of Competing Interest

The authors declare that they have no known competing financial interests or personal relationships that could have appeared to influence the work reported in this paper.

Appendix

From Eq. (12) in the main text:

$$F_a \approx m_p\left\{r\omega_1^2 \sin\beta_1 - g\cos\beta_1 + \left(r\omega_1^2\cos\beta_1 + g\sin\beta_1\right)\frac{D_p}{2a}\right\} \quad \text{(a-1)}$$

$$F_a \approx m_p\left\{r\omega_2^2 \sin\beta_2 - g\cos\beta_2 + \left(r\omega_2^2\cos\beta_2 + g\sin\beta_2\right)\frac{D_p}{2a}\right\} \quad \text{(a-2)}$$

Eliminating F_a from Eqs. (a-1) and (a-2) yields Eq. (14) in the main text:

$$a \approx \frac{D_p}{2}\cdot\frac{r\left(\omega_1^2\cos\beta_1 - \omega_2^2\cos\beta_2\right) + g(\sin\beta_1 - \sin\beta_2)}{r\left(-\omega_1^2\sin\beta_1 + \omega_2^2\sin\beta_2\right) + g(\cos\beta_1 - \cos\beta_2)} \quad (14)$$

Substituting Eq. (14) into Eq. (a-1) yields:

$$F_a = m_p\left\{(r\omega_1\omega_2)^2 + g^2\right\} \cdot \frac{(\sin\beta_2\cos\beta_1 - \cos\beta_2\sin\beta_1) + gr\left(\omega_2^2 - \omega_1^2\right)(\cos\beta_2\cos\beta_1 + \sin\beta_2\sin\beta_1)}{r\left(\omega_1^2\cos\beta_1 - \omega_2^2\cos\beta_2\right) + g(\sin\beta_1 - \sin\beta_2)} \quad \text{(a-3)}$$

Applying the addition theorem yields Eq. (13) in the main text:

$$F_a = m_p\frac{\left\{(r\omega_1\omega_2)^2 + g^2\right\}\sin(\beta_2 - \beta_1) + gr\left(\omega_2^2 - \omega_1^2\right)\cos(\beta_2 - \beta_1)}{r\left(\omega_1^2\cos\beta_1 - \omega_2^2\cos\beta_2\right) + g(\sin\beta_1 - \sin\beta_2)} \quad (13)$$

References

[1] J. Israelachvili, Intermolecular and Surface Forces, Academic Press, Santa Barbara, 2011, pp. 456–460.
[2] J. Tomas, Adhesion of ultrafine particles—A micromechanical approach, Chem. Eng. Sci. 62 (7) (2007) 1997–2010.
[3] K. Higashitani, H. Makino, S. Matsusaka, Powder Technology Handbook, 4th ed., CRC Press, Boca Raton, 2020, pp. 113–120.
[4] W.A. Ducker, T.J. Senden, R.M. Pashley, Direct measurement of colloidal forces using an atomic force microscope, Nature. 353 (6341) (1991) 239–241.
[5] Y. Shimada, Y. Yonezawa, H. Sunada, Measurement and evaluation of the adhesive force between particles by the direct separation method, J. Pharm. Sci. 92 (3) (2003) 560–568.
[6] H. Krupp, Particle adhesion theory and experiment, Adv. Colloid Interface 1 (1967) 111–239.
[7] A.D. Zimon, Adhesion of Dust and Powder, Plenum Press, New York, 1969, pp. 37–62.
[8] H. Mizes, M. Ott, E. Eklund, D. Hays, Small particle adhesion: Measurement and control, Colloids Surf. A 165 (1-3) (2000) 11–23.
[9] G.R. Salazar-Banda, M.A. Felicetti, J.A.S. Gonçalves, J.R. Coury, M.L. Aguiar, Determination of the adhesion force between particles and a flat surface, using the centrifuge technique, Powder Technol. 173 (2) (2007) 107–117.
[10] T.T. Nguyen, C. Rambanapasi, A.H. de Boer, H.W. Frijlink, P.M.v.D. Ven, J. de Vries, H.J. Busscher, K.v.D.V. Maarschalk, A centrifuge method to measure particle cohesion forces to substrate surfaces: The use of a force distribution concept for data interpretation, Int. J. Pharm. 393 (2010) 88–95.
[11] P.G.C. Petean, M.L. Aguiar, Determining the adhesion force between particles and rough surfaces, Powder Technol. 274 (2015) 67–76.
[12] M.C. Thomas, S.P. Beaudoin, An enhanced centrifuge-based approach to powder characterization: Particle size and Hamaker constant determination, Powder Technol. 286 (2015) 412–419.

[13] M.C. Thomas, S.P. Beaudoin, An enhanced centrifuge-based approach to powder characterization: Experimental and theoretical determination of a size-dependent effective Hamaker constant distribution, Powder Technol. 306 (2017) 96–102.
[14] C.A. Stevenson, M.C. Thomas, S.P. Beaudoin, An enhanced centrifuge-based approach to powder characterization: The interaction between particle roughness and particle-scale surface topography described by a size-dependent 'effective' Hamaker constant, Powder Technol. 391 (2021) 198–205.
[15] Z. JIS, 8845, Determination of Particle Adhesion Force by, Centrifugal Method (2021).
[16] F. Podczeck, J. Michael Newton, Development of an ultracentrifuge technique to determine the adhesion and friction properties between particles and surfaces, J. Pharm. Sci. 84 (9) (1995) 1067–1071.
[17] H.-C. Wang, Effects of inceptive motion on particle detachment from surfaces, Aerosol Sci. Technol. 13 (3) (1990) 386–393.
[18] S. Matsusaka, M. Koumura, H. Masuda, Analysis of adhesive force between particle and wall based on particle reentrainment by airflow and centrifugal separation, Kagaku Kogaku Ronbun 23 (1997) 561–568.
[19] K. Ilse, M.Z. Khan, K. Lange, H.N. Gurumoorthy, V. Naumann, C. Hagendorf, J. Bagdahn, Rotational force test method for determination of particle adhesion—from a simplified model to realistic dusts, J. Renew. Sustain. Energy 12 (2020) 043503.
[20] K.D.L.Á.V. Aracena, R.O. Uñac, I. Ippolito, A.M. Vidales, Movement initiation of millimeter particles on a rotating rough surface: The role of adhesion, Particuology 53 (2020) 92–99.
[21] Y. Shimada, M. Tsubota, S. Matsusaka, Measurement of particle adhesion force and effective contact radius via centrifuge equipped with horizontal and vertical substrates, Powder Technol. 397 (2022) 117103.
[22] A. Bouchoucha, S. Chekroud, D. Paulmier, Influence of the electrical sliding speed on friction and wear processes in an electrical contact copper–stainless steel, Appl. Surf. Sci. 223 (4) (2004) 330–342.
[23] J. Czarnecki, T. Dąbroś, Attenuation of the van der Waals attraction energy in the particlesemi-infinite medium system due to the roughness of the particle surface, J. Colloid Interface Sci. 78 (1980) 25–30.
[24] J. Czarnecki, V. Itschenskij, Van der Waals attraction energy between unequal rough spherical particles, J. Colloid Interface Sci. 98 (2) (1984) 590–591.